Vehicle System Dynamics
International Journal of Vehicle Mechanics and Mobility

ISSN: (Print) (Online) Journal homepage: www.tandfonline.com/journals/nvsd20

Insights into stability and control of the powerslide motion with variable drive torque distribution – applied to a driver assistance system

M. Eberhart, M. Plöchl, M. Unterreiner & J. Edelmann

To cite this article: M. Eberhart, M. Plöchl, M. Unterreiner & J. Edelmann (28 Jan 2025): Insights into stability and control of the powerslide motion with variable drive torque distribution – applied to a driver assistance system, Vehicle System Dynamics, DOI: 10.1080/00423114.2025.2457433

To link to this article: https://doi.org/10.1080/00423114.2025.2457433

VEHICLE SYSTEM DYNAMICS
https://doi.org/10.1080/00423114.2025.2457433

Insights into stability and control of the powerslide motion with variable drive torque distribution – applied to a driver assistance system

M. Eberhart[a], M. Plöchl[a], M. Unterreiner[b] and J. Edelmann[a]

[a]TU Wien, Institute of Mechanics and Mechatronics, Vienna, Austria; [b]CARIAD SE, Vehicle Motion & Energy, Wolfsburg, Germany

ABSTRACT

In this study, a theoretical investigation of the steady-state powerslide motion, or drift, is conducted to gain insight into the influence of the total drive torque and front/rear axle drive torque distribution on the powerslide dynamics of an all-wheel drive vehicle, including the case of a rear-wheel drive vehicle. The steady-state conditions and stability properties are derived, and different actuator inputs, i.e. steering angle, total drive torque and drive torque distribution, to stabilise the unstable powerslide motion are analysed and discussed with respect to different control strategies. The results indicate that the drive torque distribution is an effective control input for stabilisation and can be superior to the total drive torque input. The powerslide cannot be stabilised for particular conditions with the total drive torque input at fixed drive torque distribution. Based on these findings, a driver assistance system is presented that allows the human driver to track a desired circular path only by steering commands. The powerslide motion is stabilised automatically by a controller acting on the total drive torque and on the drive torque distribution if favourable. The characteristics, limitations in dynamics and reactions of a human driver are considered by introducing a virtual test driver model in a simulation environment. The successfully performed powerslide is shown in simulation with a basic vehicle model and in an experimental setup with a test vehicle.

ARTICLE HISTORY
Received 17 July 2024
Revised 19 November 2024
Accepted 16 January 2025

KEYWORDS
Powerslide; drifting; nonlinear vehicle dynamics; all-wheel drive vehicle; controllability; driver model

1. Introduction

The powerslide is an unstable driving condition and is defined in [1] for rear-wheel drive (RWD) vehicles as a steady-state cornering motion with a large vehicle sideslip angle and large steering angle, where the front wheels point to the outside of the turn, combined with large traction forces at the rear axle. Due to the large sideslip angle of the vehicle and large longitudinal slips at the rear tyres, there is a strong coupling between the longitudinal and lateral tyre forces. Increasing the longitudinal tyre slip by increasing the drive torque

CONTACT Manuel Eberhart manuel.eberhart@tuwien.ac.at

reduces the lateral tyre forces. Human drivers of RWD vehicles are able to use this characteristic property of the tyre to stabilise the unstable powerslide motion with the drive torque input only [2].

Even though the powerslide is an unstable steady-state driving condition, it is frequently utilised by rally drivers, particularly on loose gravel surfaces. Techniques from rally drivers, i.e. the pendulum manoeuvre and trail braking, are analysed by Velenis et al. [3]. With optimisation methods, it is shown that high sideslip manoeuvres can be advantageous in particular cases. It is demonstrated in [4–7] that for specific road conditions, the minimum time manoeuvre for a hairpin curve is characterised by large sideslip angles of the vehicle and, dependent on the drivetrain architecture of the vehicle, even countersteering may be beneficial. In [8], Acosta et al. found that large vehicle sideslip angle manoeuvres can increase manoeuvrability, and in [9], it is shown that for off-road conditions, the maximum lateral acceleration at negotiating a curve with an overactuated vehicle is achieved with large vehicle sideslip angle.

The improvement in agility can help enhance vehicle safety and improve the capability of driver assistance systems or autonomous driving applications. Autonomous vehicles typically feature a conservative driving style, and stabilisation systems usually restrict the vehicle's operation to the linear handling regime. This is typically achieved by applying differential braking. The linear regime may be extended with enhanced drivetrain architectures, particularly with electric motors and independently driven wheels. Utilising the nonlinear handling regime, including large vehicle sideslip angles, may help gain more agility in specific scenarios, e.g. to avoid obstacles. Sorniotti et al. show that obstacles could be avoided more efficiently with a large sideslip manoeuvre than by regular driving applying a nonlinear MPC approach, [10]. Zhao et al. propose in [11] a controller to improve vehicle safety by allowing large vehicle sideslips in critical situations and show in [12] that corresponding manoeuvres may prevent collisions.

Several researchers investigated the powerslide condition and the stabilisation of this unstable vehicle state. Ono et al. [13] show for a basic two degrees of freedom vehicle model that vehicle loss of stability due to oversteering at high lateral acceleration is caused by a saddle-node bifurcation. A steering control strategy is proposed to stabilise the unstable motion of the vehicle. In [14], Della Rossa et al. published an extended analysis of possible equilibria for different vehicle handling and tyre characteristics and configurations with a similar two degrees of freedom vehicle model. In [14,15], it is noted that the powerslide is an unstable saddle node. Steindl et al. found in [16] periodic limit cycles after the non-oscillatory loss of stability of the powerslide, and Edelmann et al. reveal in [17] the influence of different constant inputs on these periodic motions and present respective vehicle measurements on packed snow.

A controllability analysis of the powerslide is carried out in [2]. The authors outline that the powerslide can either be stabilised with the drive torque, the steering angle, or with both inputs for a RWD vehicle. Velenis et al. propose a sliding-mode controller with only drive and braking inputs at the front and rear axle with fixed steering to stabilise the powerslide equilibrium, [18]. In [19], an LQR-controller for a FWD vehicle with handbrake actuation is suggested with steering and drive torque as input. Controllers for stabilisation of RWD vehicles with steering and drive torque input are proposed in [20–24]. Goh et al. simultaneously stabilise the powerslide and track a given path autonomously in [25], and a model-inversion technique with wheel slip control is applied to improve the control performance in [26]. In [27], Goh et al. use a nonlinear model predictive control (NMPC) approach to perform dynamic, non-equilibrium drifting with a RWD vehicle while staying within the track limits. Front-wheel braking may be used to increase the set of possible vehicle trajectories, [28], and different controllers for overactuated vehicles with individual wheel drive are addressed in [9,29,30].

The main contribution of this paper is the analysis of the powerslide motion for an AWD vehicle with different drive torque distributions between the front and the rear axle, which has not been addressed in the literature before. An electric car with individual motors at the front and rear axle is considered, and various levels of friction potentials are included. Stability properties and possibilities to stabilise the powerslide motion are addressed by evaluating a controllability measure for different actuators which include steering angle, total drive torque and drive torque distribution. The need for a qualitative change of the control strategy for rear-wheel drive (RWD) and all-wheel drive (AWD) vehicles with fixed drive torque distribution to stabilise the powerslide is revealed and discussed. The stabilisation is shown both in simulation utilising a human driver model and in an experimental setup with the human driver in the loop. The driver's task is to track a circular trajectory with steering input only, while the powerslide motion is stabilised with a basic controller of the drive torque distribution, acting as a driver assistance system.

The remainder of this paper is organised as follows: Section 2 introduces the applied vehicle and tyre model. The system dynamics are studied in Section 3. The possible equilibria for the steady-state cornering condition are derived, and the stability and controllability properties of the powerslide conditions are discussed. Consequences on possible control strategies are addressed. Section 4 presents simulation and measurement results for a possible application in a driver assistance system. Finally, the essential outcome of the paper is briefly summarised, and conclusions are drawn.

2. Vehicle and tyre model

To investigate the impact of the drive torque distribution on the powerslide motion, in addition to the basic two-wheel vehicle model, Figure 1, the dynamics of the front and rear (substitutive) wheels are considered. Thus, the vehicle model has five degrees of freedom: vehicle velocity v, sideslip angle of the vehicle β, yaw rate $\dot{\psi}$, and angular velocities of the front and rear wheels ω_F and ω_R, respectively. The equations of motion of the basic two-wheel vehicle model read

$$m\dot{v}\cos\beta - mv(\dot{\beta} + \dot{\psi})\sin\beta = F_{xF}\cos\delta - F_{yF}\sin\delta + F_{xR} \tag{1}$$

$$m\dot{v}\sin\beta + mv(\dot{\beta} + \dot{\psi})\cos\beta = F_{xF}\sin\delta + F_{yF}\cos\delta + F_{yR} \tag{2}$$

$$\ddot{\psi} I_z = (F_{xF}\sin\delta + F_{yF}\cos\delta)l_F - F_{yR}l_R \tag{3}$$

with the vehicle mass m, the steering angle δ, the distances l_F and l_R from the centre of gravity CG to the front and rear axle, the yaw moment of inertia of the vehicle I_z, the longitudinal axle/tyre forces F_{xF} and F_{xR}, and the lateral axle/tyre forces F_{yF} and F_{yR}. The axle/wheel dynamics at the front and rear axles are described by

$$I_F\dot{\omega}_F = T_F - rF_{xF} \quad \text{and} \quad I_R\dot{\omega}_R = T_R - rF_{xR} \tag{4}$$

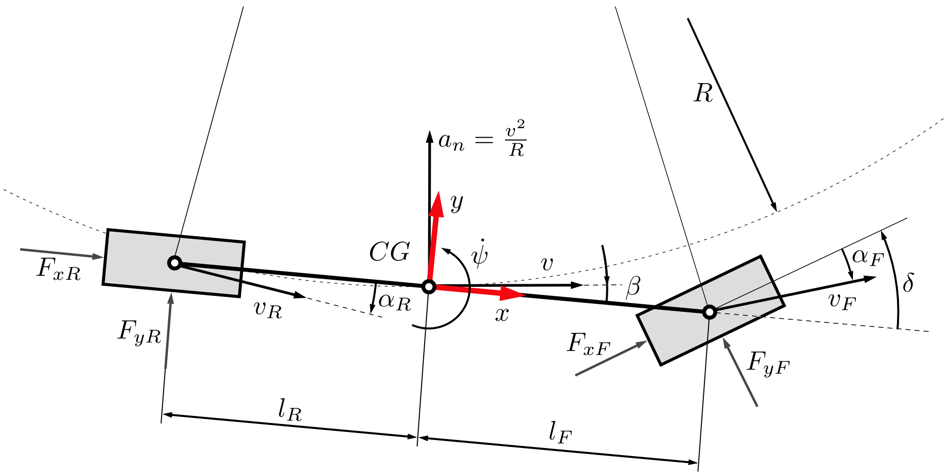

Figure 1. Two-wheel vehicle model at regular cornering.

with the angular velocities ω_F and ω_R, the effective moments of inertia I_F and I_R, the drive torques T_F and T_R, and the loaded radius r, which is considered constant and equal to the effective rolling radius.

To map the powerslide handling regime, not only the complete set of nonlinear system Equations (1)–(4) has to be considered, but also the mutual influence of longitudinal and lateral tyre forces. The *Magic Formula* tyre model [31] is applied here.

The respective sideslip angles α_i and longitudinal slips s_{xi} of the tyres read

$$\alpha_F = \delta - \arctan\left(\frac{\dot{\psi} l_F}{v\cos\beta} + \tan\beta\right) \quad \text{and} \quad \alpha_R = -\arctan\left(-\frac{\dot{\psi} l_R}{v\cos\beta} + \tan\beta\right), \tag{5}$$

$$s_{xF} = -\frac{v_{wF} - \omega_F r}{v_{wF}} \quad \text{and} \quad s_{xR} = -\frac{v\cos\beta - \omega_R r}{v\cos\beta} \tag{6}$$

with the longitudinal velocity of the front tyre

$$v_{wF} = v\cos\beta\cos\delta + (v\sin\beta + \dot{\psi} l_F)\sin\delta. \tag{7}$$

As different front and rear tyres are considered, Figure 2 depicts the normalised combined longitudinal and lateral tyre forces for varied tyre sideslip angles α_i for the front and rear tyres at the constant nominal tyre loads $F_{zF} = 6000$ N and $F_{zR} = 6250$ N. The tyre parameters are fitted to measurement data to achieve the desired handling characteristics of a reference vehicle, also taking the steering system compliance into account. Vehicle model parameters are listed in Table 1.

3. System dynamics analysis

To gain insight into the system dynamics of the powerslide, the steady-state solution branches of the system model are derived first. The influence of the tyre–road friction potential and the drive torque distribution on the steady-state solution branches are examined, and the corresponding stability properties and the effectiveness of different control inputs to stabilise the unstable powerslide solution branch are studied.

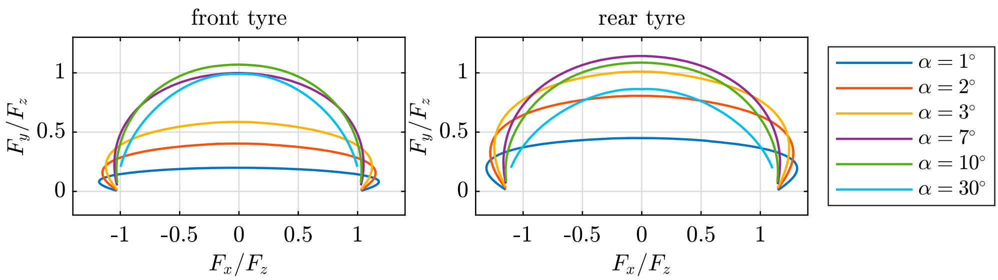

Figure 2. Combined tyre forces in the longitudinal and lateral direction for different sideslip angles α and tyre–road friction potential $\mu = 1$.

Table 1. Parameters of the two-wheel vehicle model.

Parameter	Abbr.	Value	Unit
Vehicle mass	m	2500	kg
Yaw moment of inertia	I_z	3600	kgm^2
Front axle inertia	I_F	6.5	kgm^2
Rear axle inertia	I_R	40	kgm^2
Front axle distance $\overline{CG\,F}$	l_F	1.48	m
Rear axle distance $\overline{CG\,R}$	l_R	1.42	m
Eff. rolling/loaded radius	r	0.36	m

3.1. Steady-state solution branches

The nonlinear equations of motion in (1)–(4) are written in state-space notation

$$\dot{\mathbf{x}} = \mathbf{f}(\mathbf{x}, \mathbf{u}) \tag{8}$$

with the state vector $\mathbf{x} = [\beta, \dot{\psi}, v, \omega_F, \omega_R]^{\mathrm{T}}$ and input vector $\mathbf{u} = [\delta, T_{\text{tot}}, \gamma\,]^{\mathrm{T}}$ with total drive torque $T_{\text{tot}} = T_F + T_R$ and drive torque distribution $\gamma = T_R/T_{\text{tot}}$, defined as the portion of the total drive torque at the rear axle. The steady-state solution branches of the system (8) are numerically calculated by setting $\dot{\mathbf{x}} = \mathbf{0}$ and $\dot{\psi} = v/R$ with constant radius of curvature R.

For the handling diagram in Figure 3, the vehicle sideslip angle β, the steering angle δ and the total drive torque T_{tot} are plotted over the normal acceleration $a_n = v^2/R$. Therefore, a radius of curvature with $R = 60$ m, a tyre–road friction potential with $\mu = 1$, and a drive torque distribution with $\gamma = 0.8$ have been assumed. Similar to [1], up to four different steady-state solutions are found for a particular vehicle velocity v and radius of curvature R.

Besides regular cornering ①, with small positive steering angle δ, small vehicle sideslip angle β, and small total drive torque T_{tot}, there are two additional branches, ② and ④, denoted overdraw steering, with larger positive steering angle δ and therefore larger sideslip angle α_F at the front axle w.r.t. regular cornering.

The first overdraw steering branch ② appears when, due to the friction limit of the front tyre, the maximum lateral acceleration a_n is reached, and the steering angle is further increased. The sideslip angle α_F at the front axle increases while the vehicle sideslip angle β remains almost the same w.r.t. regular cornering.

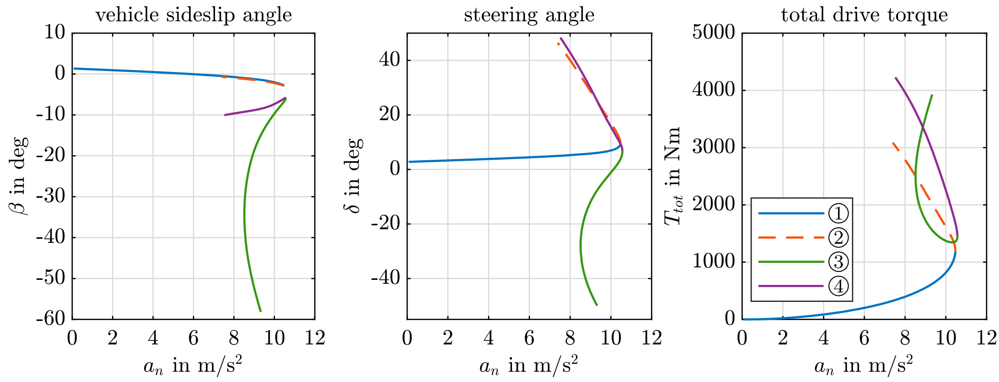

Figure 3. Steady-state solutions of the two-wheel vehicle model (①: regular cornering, ②: overdraw steering 1, ③: powerslide, ④: overdraw steering 2) for radius $R = 60$ m, tyre–road friction potential $\mu = 1$, and drive torque distribution $\gamma = 0.8$.

For the second overdraw steering branch ④, the vehicle sideslip angle β shows a decreased but rather constant negative value of about $\beta \approx -8^\circ$, while the sideslip angle of the front axle α_F increases with decreasing normal acceleration. The required total drive torque for both overdraw steering solutions increases with the steering angle δ due to the higher cornering resistance.

The powerslide branch ③ shows large negative vehicle sideslip angles β, large negative steering angles δ, and large total drive torques T_{tot}. It becomes evident from Figure 3 that the powerslide branch joins the second overdraw steering branch ④. In contrast to ④, the lateral tyre forces of the front axle are not saturated. Since Figure 3 corresponds to a left turn with a positive yaw rate $\dot{\psi}$ according to Figure 1, the negative steering angle δ indicates that the front wheels point to the outside of the curve, called countersteering.

Due to large sideslip angles α_R and large longitudinal forces F_{xR} at the rear axle, the corresponding tyre forces are saturated at the powerslide branch ③. As a result of the mutual influence of longitudinal and lateral tyre forces, a strong coupling between the longitudinal and lateral dynamics of the vehicle can be expected, see subsequent Section 3.3. Moreover, this mutual influence may be helpful in the control and stabilisation task of the powerslide motion, see Sections 3.4 and 3.5.

3.2. Variation of friction potential and drive torque distribution

For a decreasing friction potential μ of the tyre–road contact, the steady-state powerslide branch is shifted to lower normal accelerations a_n, as depicted in Figure 4(a), while its general shape remains similar.

By examining the required total drive torque T_{tot} for a steady-state powerslide at different vehicle sideslip angles β and tyre–road friction potentials μ, an almost linear relationship between the resulting normal acceleration $a_n = a_n(\beta, \mu)$ and the total drive torque T_{tot} appears, just as between the vehicle sideslip angle β and the total drive torque T_{tot}, Figure 4(b).

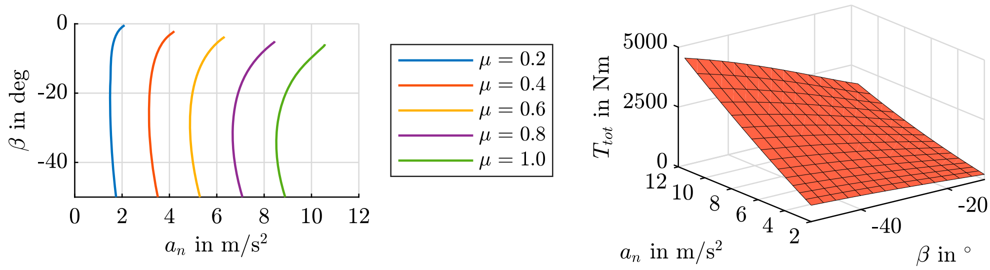

Figure 4. Steady-state solutions of the powerslide branch for different tyre–road friction potentials and required total drive torque ($R = 60$ m, $\gamma = 0.8$). (a) Powerslide branches for different tyre–road friction potentials μ and (b) Total drive torque T_{tot} depending on normal acceleration a_n and vehicle sideslip angle β.

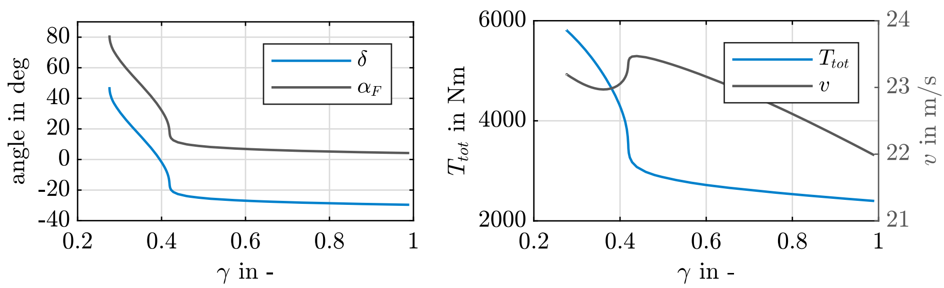

Figure 5. Steady-state solutions of the powerslide branch for different drive torque distributions γ at the constant vehicle sideslip angle $\beta = -35°$. (a) Steering angle δ and sideslip angle at the front axle α_F and (b) Total drive torque T_{tot} and velocity v.

To learn about the existence and characteristic properties of the powerslide for different drive torque distributions γ, all steady-state solutions for constant vehicle sideslip angles β are calculated for γ reduced from $\gamma = 1$ towards 0 until no powerslide solution exists.

For the chosen constant vehicle sideslip angle $\beta = -35°$, steady-state solutions for the considered vehicle parameters are found in the range from $\gamma = 1$ (rear-wheel drive) to the most 'front-oriented' drive torque distribution of $\gamma \approx 0.27$, see Figure 5. From $\gamma = 1$ until $\gamma \approx 0.43$ slightly increasing, large negative steering angles δ result, typical for the powerslide motion with a rear-wheel drive vehicle, [1]. Also, the sideslip angle of the front axle α_F, the total drive torque T_{tot}, and the vehicle velocity v slightly increase in this range until the maximum velocity is reached at $\gamma \approx 0.43$. In contrast, at drive torque distributions $\gamma < 0.43$, considerably less countersteering is required until regular steering (positive steering angle) is necessary for $\gamma < 0.39$. The need for considerably smaller negative or even positive steering angles δ when drifting all-wheel drive vehicles compared with rear-wheel drive vehicles is well known from anecdotal evidence and observations. Moreover, a strong increase of the total drive torque T_{tot} is observed for $\gamma < 0.43$. This increase may be attributed to the degraded lateral tyre force potential at the front axle from the mutual influence of lateral and longitudinal tyre forces, resulting in very large sideslip angles α_F and increased steering angles δ, and corresponding energy dissipation.

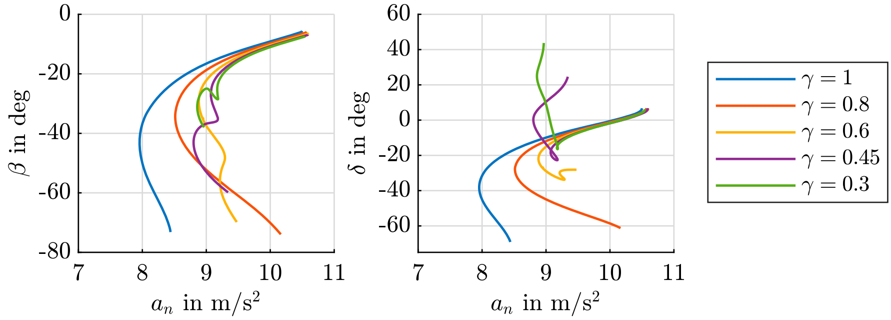

Figure 6. Vehicle sideslip angle β and steering angle δ of the powerslide branch for different drive torque distributions γ ($R = 60$ m, $\mu = 1$).

The handling diagrams for different constant drive torque distributions γ are shown in Figure 6. For larger values of γ, the characteristics of the powerslide branches for vehicle sideslip angle and steering angle are similar as for rear-wheel drive vehicles. Decreasing values of γ further, results in a change of the characteristics, as front tyre forces become saturated as well. For certain vehicle velocities v and drive torque distributions γ, up to four powerslide equilibria can be identified for a given radius of curvature ρ and normal acceleration a_n, see, for example, $\gamma = 0.6$ in Figure 6(right). Moreover, at more front-orientated drive torque distributions, e.g. $\gamma = 0.45$, where vehicle sideslip angles β are still large and negative, steering angles δ may be positive, indicating regular steering, similar to Figure 5(a). Consequently, in contrast to RWD vehicles, counter-steering may not be required to maintain a steady-state powerslide for AWD vehicles, depending on the drive torque distribution γ. Considering a given vehicle sideslip angle β, up to three powerslide equilibria can be identified for a constant drive torque distribution γ, each associated with a different normal acceleration a_n and steering angle δ, see e.g. $\gamma = 0.3$ in Figure 6(left). Obviously, smaller values of γ result in higher normal accelerations a_n.

3.3. Stability of first order and modal analysis

Linearisation of the nonlinear system equations at the steady-state solution branches results in $\Delta\dot{\mathbf{x}} = \mathbf{A}\Delta\mathbf{x} + \mathbf{B}\Delta\mathbf{u}$ with system matrix $\mathbf{A}$ and input matrix $\mathbf{B}$. $\Delta\mathbf{x} = \mathbf{x} - \mathbf{x}_0$ is the deviation of the state vector and $\Delta\mathbf{u} = \mathbf{u} - \mathbf{u}_0$ the deviation of the input vector from the steady-state solution, indicated by index 0. For the sake of simplicity, Δ-symbols and 0-indices have been omitted below. By solving the eigenvalue problem $(\mathbf{A} - \mathbf{I}\lambda_i)\mathbf{p}_i = \mathbf{0}$ for eigenvalues λ_i and right eigenvectors $\mathbf{p}_i$ corresponding to mode i ($i = 1$–5), the local dynamic behaviour and stability of the steady-state solutions can be analysed.

The vehicle shows understeering characteristics at the regular cornering branch 1 in Figure 3, the eigenvalues are all negative, and steady-state solutions are stable. The eigenvalues of the connecting first overdraw steering branch 2 have only negative real parts as well, and also these steady-state solutions are stable. For the regular cornering branch, the largest eigenvalue always remains real but still negative and very close to zero; see also [1]. The main entries in the corresponding right eigenvector are related to velocity v and angular velocities of the front and rear wheels, ω_F and ω_R, and therefore can be associated with a 'velocity mode'. The next two eigenvalues change from real to a conjugate-complex pair

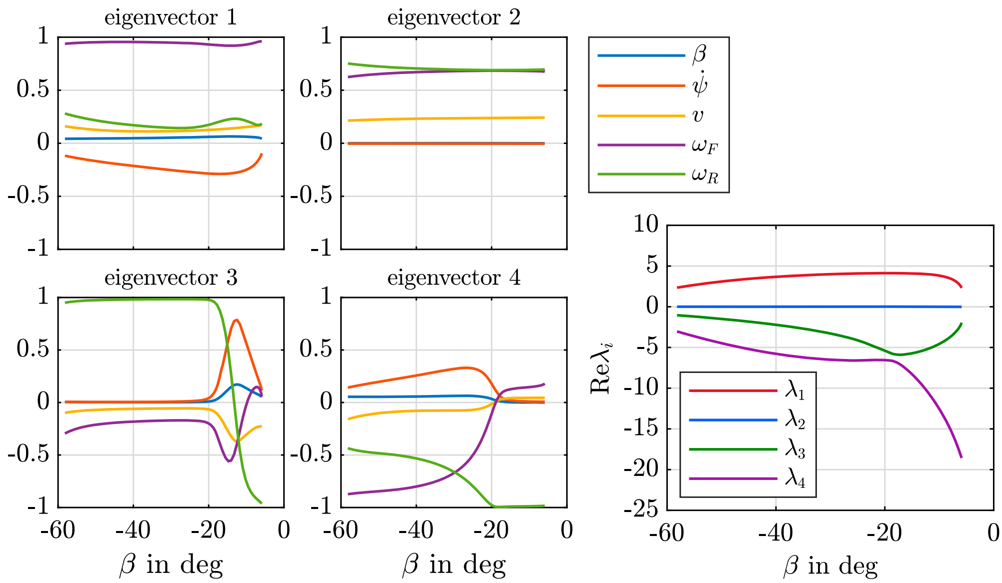

Figure 7. Dominant eigenvectors and eigenvalues corresponding to the powerslide branch ③ in Figure 3.

of eigenvalues with increasing velocity v. The oscillation mode remains for the first overdraw steering branch ②, with main contributions to yaw rate $\dot{\psi}$ and vehicle sideslip angle β, affecting the lateral motion of the vehicle. The two remaining eigenvalues are largely negative, and the largest entries of the corresponding eigenvectors are mainly related to the angular velocities of the front and rear wheels, ω_F and ω_R.

For the powerslide branch ③ in Figure 3, the eigenvalues λ_i $(i = 1-4)$ and the entries in the corresponding (normalised) eigenvectors $\mathbf{p}_i$ are plotted over the vehicle sideslip angle β in Figure 7. Index 1 refers to the largest and positive eigenvalue, index 4 to the smallest, negative eigenvalue. Less interesting λ_5 and $\mathbf{p}_5$ are not shown, the eigenvalue is largely negative, and its eigenvector has a main component in the angular velocity of the front wheel ω_F.

In contrast to regular cornering, the eigenvalues of powerslide branch are always real. The real eigenvalues λ_1 and λ_2 are positive over the full range of vehicle sideslip angles β. Hence, the corresponding steady-state solutions are unstable, and the loss of stability is monotonic and governed by mode 1, see also [1], since λ_2 is very close to zero, quite similar to the 'velocity mode' at the regular cornering branch. The entries in the eigenvectors corresponding to λ_1 remain almost constant over the full range of vehicle sideslip angles β and affect all states, see Figure 7 on the left, with the largest contributions to the angular velocity of the front wheel ω_F and the yaw rate $\dot{\psi}$.

The non-oscillatory and similar behaviour over the full vehicle sideslip range could be beneficial for the control and stabilisation task of the driver, considering the limitations of a human driver [32]. Since the contribution to the yaw rate $\dot{\psi}$ remains quite large compared to the other 'modes', this unstable mode may be denoted 'yaw mode'.

A qualitative change in the course of entries in the eigenvectors of mode 3 and 4 can be observed at $\beta \approx -20^\circ$, Figure 7, where the magnitudes of the real eigenvalues λ_3 and

λ_4 come quite close. For vehicle sideslip angles $\beta < -20°$, the angular velocity of the rear wheel ω_R is dominant in the eigenvector of mode 3, and for $\beta > -20°$ in the eigenvector of mode 4. The eigenvalue λ_4 for $\beta > -20°$ and λ_3 for $\beta < -20°$ (in the areas where the angular velocity of the rear wheel ω_R is dominant) strongly depends on the rear axle inertia I_R. A lower rear axle inertia would shift these eigenvalues to lower values and therefore the location of the qualitative change of the mode shapes to lower vehicle sideslip angles. A large decrease in the rear axle inertia I_R would even prevent the change of mode shape.

Following the powerslide branch, the second overdraw steering branch ④ in Figure 3 appears with increasing steering angles δ after passing the maximum normal acceleration a_n. The second overdraw steering branch also corresponds to unstable steady-state solutions. The modes are qualitatively similar to the powerslide modes for small vehicle sideslip angles β, where again the real eigenvalue λ_1 related to the 'yaw mode' is positive and the real eigenvalue λ_2 related to the 'velocity mode' is negative. In contrast to the powerslide solutions, the lateral tyre force at the front axle is saturated.

Variation of the tyre–road friction potential in the range $\mu = 0.2 - 1$ reveals for the powerslide branch that the friction potential has no qualitative impact on the dynamic behaviour. The eigenvalue of the unstable mode 1 decreases slightly with reduced friction potential. A similar result is found by varying the drive torque distribution between $\gamma = 0.6 - 1$. The largest (positive) eigenvalue decreases slightly with decreasing γ.

3.4. Controllability analysis of the powerslide motion

As shown in [2], the powerslide of a RWD vehicle can either be stabilised with the drive torque at the rear axle, with the steering angle, or with a combination of both commands. The effectiveness of the different inputs to control the steady-state regular cornering and powerslide motion with respect to sensed vehicle states has been evaluated by a gross measure of joint modal controllability and observability. It provides an idea of how a mode is affected by a specific input and how visible it is from a specific output of the locally linearised system model. The measure was introduced by Hamdan et al. [33]. Choi et al. applied a modified version in [34] by taking the length of the input vector $|\mathbf{b}_j|$ of input j from input matrix $\mathbf{B}$ into account. In this work, the measure is further extended by considering the range of operation of each actuator by scaling the modal controllability measure with the maximum input of the actuator.

The subsequent measure of modal controllability of mode i with input j is the cosine of the angle between the left eigenvector $\mathbf{q}_i$ (from $\mathbf{A}^{\mathrm{T}}\mathbf{q}_i = \lambda_i\mathbf{q}_i$) and input vector $\mathbf{b}_j$ scaled with the norm of the input vector $|\mathbf{b}_j|$ and the maximum input $u_{j,\max}$ of actuator j. This measure can be interpreted as the projection of the input vector $\mathbf{b}_j$ on the left eigenvector $\mathbf{q}_i$ normalised to length 1, scaled with $u_{j,\max}$ and yields

$$M_{c,ij} = \cos\theta_{ij}|\mathbf{b}_j|u_{j,\max} \quad \text{with} \quad \cos\theta_{ij} = \frac{\mathbf{q}_i^{\mathrm{T}}\mathbf{b}_j}{|\mathbf{q}_i||\mathbf{b}_j|}. \tag{9}$$

Here, the maximum input $u_{j,\max}$ is set to $u_{\delta,\max} = \pi/4$ for the steering angle δ, $u_{T_{\mathrm{tot}},\max} = 5000$ for the total drive torque T_{tot}, and $u_{\gamma,\max} = 1$ for the drive torque distribution γ. As a measure for the modal observability of mode i from output k, the projection of the right

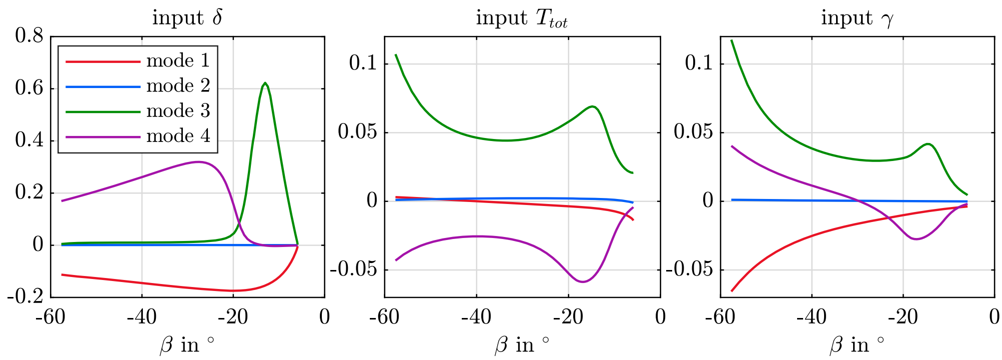

Figure 8. Joint modal controllability and observability measure $M_{co,j\beta}$ for inputs $j = \{\delta, T_{\text{tot}}, \gamma\}$ and observed vehicle sideslip angle β for the powerslide branch ③ in Figure 3.

eigenvector $\mathbf{p}_i$ on the output vector $\mathbf{c}_k$ from output matrix $\mathbf{C}$ is applied,

$$M_{o,ki} = \cos\theta_{ki}|\mathbf{c}_k| \quad \text{with} \quad \cos\theta_{ki} = \frac{\mathbf{c}_k\mathbf{p}_i}{|\mathbf{p}_i||\mathbf{c}_k|}. \tag{10}$$

The product of these two measures

$$M_{co,jk} = M_{o,ki}M_{c,ij} \tag{11}$$

provides insight into the effectiveness of specific actuator input–measured output combinations to control a specific mode and thus stabilise the unstable powerslide equilibrium.

The measure in (11) is now evaluated for the steady-state powerslide branch ③ in Figure 3 ($R = 60$ m, $\mu = 1$, and $\gamma = 0.8$) for the inputs δ, T_{tot} and γ, and output β. Figure 8 shows the measure $M_{co,j\beta}$ for the first four modes, plotted over the steady-state vehicle sideslip angle β (actually β_0 for clearness). Since the linear analysis is only valid in the vicinity of the steady-state solutions of the nonlinear powerslide branch, the results have to be interpreted with care.

The left plot of Figure 8 shows that the unstable mode 1 can be controlled very effectively with the steering angle δ for the full range of considered vehicle sideslip angles β. In the range of vehicle sideslip angles where ω_R is the dominant entry in the eigenvector of modes 3 and 4, see Figure 7, the possibility to influence these modes with the steering angle δ almost vanishes, whereas controllability is given in the range of vehicle sideslip angles β where the yaw rate $\dot{\psi}$ is the dominant entry. Mode 2, which represents the 'velocity mode', can hardly be controlled by the steering angle.

For the total drive torque input T_{tot} an interesting observation can be made, middle plot of Figure 8. The joint modal measure for the unstable mode 1 is about zero for vehicle sideslip angles $\beta \approx -40°$ and also changes its sign for further decreasing β. Thus, in this specific condition, the unstable mode cannot be controlled. This observation and the consequences of the change of the sign of the measure will be discussed in more detail below. Modes 3 and 4 that are basically dominated by the yaw and rear axle motion, $\dot{\psi}$ and ω_R, respectively, can be influenced well with input T_{tot}, whereas the measure remains again small for the 'velocity mode' 2 for the full range of vehicle sideslip angles β.

In the right plot of Figure 8, the modal measure is presented for the drive torque distribution γ. The possibility to influence the unstable mode 1 rises with decreasing vehicle

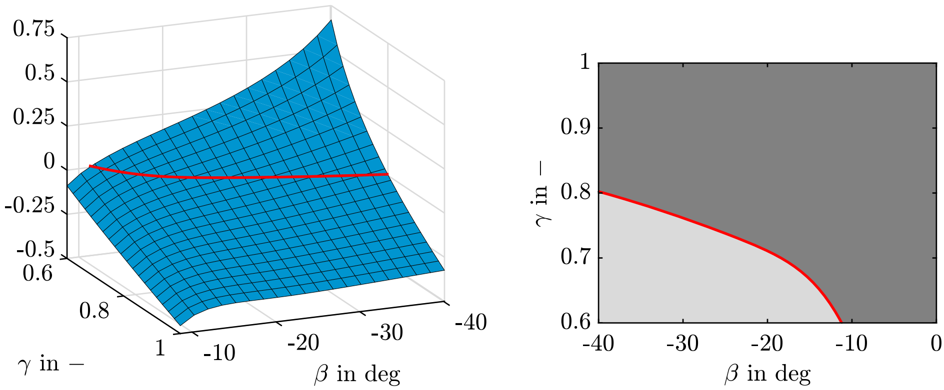

Figure 9. Modal controllability measure $M_{c,1T_{\text{tot}}}$ for input T_{tot} and mode 1 ($\mu = 1$). (a) $M_{c,1T_{\text{tot}}}$ for different vehicle sideslip angles β and drive torque distributions γ and (b) Projection to the β–γ plane: qualitative change of the control strategy at $M_{c,1T_{\text{tot}}} = 0$ (red line).

sideslip angles β. The influence of γ on mode 3 is high and almost zero on the 'velocity mode', similar to the influence of the steering input δ. For mode 4, the measure also exhibits zero-crossing. However, this is not relevant since the real eigenvalue related to mode 4 is negative.

Similar results as shown in Figure 8 are found for different tyre–road friction potentials μ.

To gain more insight into the change of the sign of the joint modal controllability and observability measure $M_{co,T_{\text{tot}}\beta}$ for the input total drive torque T_{tot} of the unstable mode 1, Figure 8, the associated modal controllability measure $M_{c,1T_{\text{tot}}}$ in (9), is shown for different vehicles sideslip angles β and drive torque distributions γ in Figure 9(a).

It can be noticed that there are combinations of drive torque distributions γ and vehicle sideslip angles β where $M_{c,1T_{\text{tot}}}$ crosses zero and changes its sign. The term $\cos\theta_{1T_{\text{tot}}}$ in (9) becomes zero, when the angle between the input vector $\mathbf{b}_{T_{\text{tot}}}$ and the left eigenvector $\mathbf{q}_1$ related to mode 1 are orthogonal to each other. After transition through $M_{c,1T_{\text{tot}}} = 0$ for e.g. varied β and fixed γ, the control command (w.r.t. the steady-state input) changes sign for a similar yaw response considering the unstable, dominant 'yaw mode' of the powerslide equilibrium, which is associated with a change of control strategy. Therefore, the required (strategy for the) control of the total drive torque T_{tot} to stabilise the powerslide mode at large negative vehicle sideslip angles β, will strongly depend on the drive torque distribution γ, see Figure 9(b).

Consequently, the control strategies may be distinguished by the drive train configuration between '*RWD-strategy*' and '*AWD-strategy*'. The assumed distinction coincides with anecdotal knowledge from expert drivers, who report that a RWD vehicle can be controlled easily by drive torque commands (corresponding to T_{tot}), since increased drive torque results in increased longitudinal slip s_{xR} and reduced lateral tyre forces F_{yR} at the rear axle, and therefore increased yaw rate $\dot{\psi}$, and vice versa. In contrast, at AWD vehicles, the increased drive torque T_{tot} results also in additional longitudinal tyre forces F_{xF} at the front axle that overcompensate the effects from the reduced lateral tyre forces F_{yR} at the rear axle, hence the yaw rate $\dot{\psi}$ decreases. The areas of different control strategies in the

γ–β plane are illustrated in Figure 9(b) in dark grey colour for '*RWD-strategy*' and light grey colour for '*AWD-strategy*'.

3.5. Control strategy

The loss of controllability with the total drive torque T_{tot} in particular situations in contrast to the drive torque distribution γ suggests that γ or individual axle torques are proper inputs to stabilise the powerslide, or might even be superior to the total drive torque T_{tot} with fixed torque distribution γ. Therefore, a control strategy that stabilises the powerslide motion just with the drive train, in particular of an AWD vehicle, is addressed in this section. The steering angle shall be left for the control of the circular path.

The analysis with the joint modal controllability and observability measure, Figure 8, has revealed that the vehicle sideslip angle β and the yaw rate $\dot{\psi}$ are proper measurement variables for a controller, with the last being even more effective for influencing the unstable powerslide or 'yaw mode'. However, as there is only a marginal effect on the unstable 'velocity mode', further measurement variables related to the longitudinal motion are required, such as velocities v, ω_F, ω_R, which show a strong effect on the 'velocity mode'. In agreement with the evaluation of the controllability criteria from Kalman and Hautus [35], the unstable eigenvalues can be stabilised, and the dynamics chosen favourably by placing the eigenvalues of the closed-loop, respectively, using the full state vector as a measurement vector.

However, to mimic a human driver, only the observed vehicle sideslip angle and yaw rate will now be considered as measurement variables. The idea is motivated by Goh et al. [26], who state that the vehicle velocity v does not need to be explicitly regulated even though the variable $\dot{v}$ is uncontrolled as the coupling between the lateral and the longitudinal dynamics that occurs at high sideslip stabilises the velocity when operating under their imposed control law. It is interesting to note that these findings hold for their vehicle with RWD, but not necessarily for an AWD vehicle.

For illustration, the system model is linearised w.r.t. $\beta = -35^\circ$ and a constant output feedback controller is considered to stabilise the steady-state powerslide equilibrium with input T_{tot} and outputs $\dot{\psi}$ and β. The controller gains are denoted $K_{\dot{\psi}}$ and K_β, respectively. The real parts of the largest eigenvalue of the controlled system are calculated for a wide range of control gains K_β and $K_{\dot{\psi}}$ and plotted for configurations $\gamma = 1$ (RWD) and $\gamma = 0.6$ (AWD) in Figure 10.

For $\gamma = 1$ (RWD) the largest eigenvalue can be moved into the negative half-plane for specific control gains. In contrast, for $\gamma = 0.6$ (AWD), the largest eigenvalue remains positive and the equilibrium unstable for all combinations of gains $K_{\dot{\psi}}$ and K_β. Both systems are controllable, except for drive torque distributions γ on the red line in Figure 9(b). However, the limited number of two controller design parameters only does not allow the five poles to be placed freely. Nevertheless, the RWD vehicle can still be stabilised, but not the AWD vehicle at $\gamma = 0.6$. For small enough γ, close to the limit of existing powerslide motions, stabilisation with this reduced control design space will be possible again.

When aiming to reduce the real part of the largest eigenvalue by a proper choice of K_β, signs of K_β are opposite for the two drive train configurations, Figure 10, confirming the above-mentioned different control strategies to stabilise the powerslide motion at RWD or

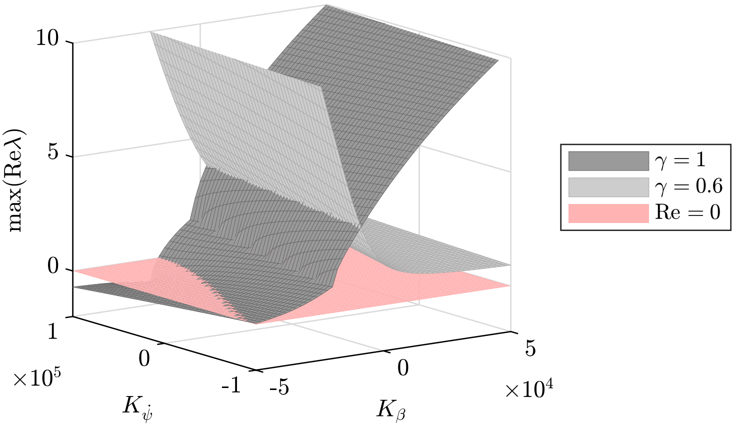

Figure 10. Maximum real part of the largest eigenvalue of the controlled system with gains $K_{\dot{\psi}}$ and K_β.

AWD vehicles. For RWD vehicles, the total drive torque T_{tot} needs to be reduced to diminish the vehicle sideslip angle β, and also the vehicle velocity v will be reduced accordingly ('*RWD-strategy*'). For γ in the light grey area of Figure 9(b), the total drive torque T_{tot} needs to be increased to diminish the vehicle sideslip angle β, and therefore the vehicle velocity v will also increase ('*AWD-strategy*').

In conclusion, for AWD vehicles with specific constant drive torque distributions γ, the unstable eigenvalue related to the 'yaw mode' can be stabilised with the above controller. Still, one eigenvalue related to the 'velocity mode' remains unstable. Although the 'velocity mode' is also (slightly) unstable at RWD vehicles, the vehicle velocity converges to its equilibrium state when the vehicle sideslip angle is stabilised by the total drive torque due to the velocity zero-dynamics, [26]. But for AWD vehicles, the total drive torque to stabilise the unstable 'yaw mode' and thus the vehicle sideslip angle does not automatically stabilise the unstable 'velocity mode', indicating possibly unstable zero-dynamics. This result coincides with findings from [36], based on a phase-plane analysis of the powerslide motion.

As a consequence, it is assumed, when utilising a constant output controller with the vehicle sideslip angle as a measurement variable, having the right graph of Figure 8 in mind, that the powerslide motion could be stabilised for AWD vehicles with a variable drive torque distribution. In this way, with large γ, the benefit from a stable 'velocity mode' and with small γ, the benefit from a direct yaw moment due to the longitudinal tyre forces at the front axle can be combined. The feasibility of this approach is now tested in a particular application case.

4. Application: driver assistance system

Based on the above analysis of the powerslide branch ③ in Figure 3 and the effectiveness of the investigated control inputs, a basic driver assistance system to perform a steady-state powerslide is proposed in this section. The task of this driver assistance system is to stabilise the powerslide motion by shifting the total drive torque between the front and rear axle, where the human driver has to track the circular path only by utilising steering commands.

In contrast to previous work, e.g. [9,24,26], which focuses on autonomous drifting, the human driver is included in the control loop.

Considering the conclusions from Sections 3.4 and 3.5, a variable drive torque distribution γ is used to stabilise the steady-state powerslide motion. The nominal drive torque distribution γ_0 is selected in the range $\gamma_0 = 0.5 - 0.9$ for powerslide steering behaviour with a negative steering angle and small sideslip angle at the front axle α_F according to Figure 5. The total drive torque $T_{\text{tot},0}(\beta_{\text{des}}, \mu, \gamma_0)$ is pre-selected to adjust to a desired vehicle sideslip angle β_{des} for a given tyre–road friction potential μ and nominal drive torque distribution γ_0, see Figures 4(b) and 5 in Section 3.2.

A simple PD-controller is chosen to move the eigenvalue of the unstable mode 1, Figure 7 in Section 3.3, to the negative half-plane by controlling the drive torque of the front and rear axle, T_F and T_R,

$$T_F = T_{\text{tot},0}(1 - \gamma_0) + a_1 e_\beta + a_2 \dot{e}_\beta \tag{12a}$$

$$T_R = T_{\text{tot},0}\gamma_0 - a_1 e_\beta - a_2 \dot{e}_\beta \tag{12b}$$

with the vehicle sideslip angle error $e_\beta = \beta - \beta_{\text{des}}$ and its derivative $\dot{e}_\beta$, and the control gains a_1 and a_2. Since (regenerative) braking is not considered, the lower boundary for the axle drive torques is zero. If this boundary is reached, the total drive torque T_{tot} can be increased by the driver assistance system (limited by the maximum motor torque) for better tracking performance of the controller at large disturbances. The availability of regenerative braking would be favourable in this respect.

4.1. Human driver model – virtual test driver

To investigate the driver assistance system in the simulation environment, first, its interaction with a human driver is considered by adapting the virtual two-layer test driver model described in [37]. The steering angle $\delta = \delta_{ff} + \delta_c + \delta_{cs}$ is composed of the steering angle δ_{ff} from anticipation, the steering angle δ_c from disturbance compensation, and the steering angle δ_{cs} from countersteering. Since the anticipated curvature κ of the track remains constant for the circular path, the *anticipatory feed-forward layer* results in the constant steering angle $\delta_{ff} = \delta_{ff,0}$ corresponding to the regular cornering manoeuvre before the powerslide is initiated.

The predictive *compensatory closed-loop layer* $G_c(s)$ compensates the predicted (with preview time T_p) path deviation Δy with the steering input δ_c,

$$G_c(s) = \frac{\delta_c(s)}{\Delta y(s)} = K_c \frac{1 + T_v s}{1 + T_n s} e^{-s\tau}, \tag{13}$$

with driver gain K_c and time constants T_v and T_n. The human reaction time is chosen constant $\tau = 0.2\,\text{s}$, [38]. $T_n = 0.14\,\text{s}$, $T_v = 3.6\,\text{s}$, $T_p = 0.3\,\text{s}$, and $K_c = 0.013\,\text{rad/m}$ are found by applying the 'cross-over' assumption, [38], for the considered vehicle and tyre model, Table 1 and Figure 2, at regular cornering for a normal acceleration of $a_n = 8\,\text{m/s}^2$.

As the vehicle increases in sideslip, after the powerslide manoeuvre has been initiated, the driver applies countersteer, which effectively reduces the tyre sideslip angle at the front wheels and the yaw moment, until no net yaw moment is produced, [39]. Then, the vehicle is stabilised at the desired vehicle sideslip angle, and there results a small offset between steering angle and vehicle sideslip angle. The countersteer task after the initiation of the powerslide manoeuvre is represented by an additional *countersteer layer* imposing a (human) lag steering behaviour $\Delta\delta_{cs}$

$$G_{cs}(s) = \frac{\delta_{cs}(s)}{\Delta\beta(s)} = K_{cs}\frac{1}{1+T_1 s}e^{-s\tau} \tag{14}$$

with time constant $T_1 \approx T_n$ and K_{cs} to finally match the steering angle of the demanded powerslide equilibrium. $\Delta\beta$ is the developing deviation of the current vehicle sideslip angle from the vehicle sideslip angle at initial regular cornering.

4.2. Simulation

A simulated powerslide manoeuvre of the closed-loop 'vehicle–driver–driver assistance system', utilising the vehicle model described in Section 2 and the driver model and the driver assistance system described in Section 4, is shown in Figure 11. The virtual test driver tracks a circular path with radius $R = 60$ m on a surface with tyre–road friction potential $\mu = 1$. Starting in regular driving condition, the powerslide is initiated at time $t = 5$ s by setting up a demanded vehicle sideslip angle ramp to $\beta_{\text{des}} = -35^{\circ}$ with a rate of $10^{\circ}/\text{s}$. The left top plot in Figure 11 shows this ramp. The controller is able to track the demanded vehicle sideslip angle very well. During the initialisation phase, the controller shifts all drive torque to the rear until the maximum total drive torque is reached, left bottom plot, resulting in large traction forces at the rear axle, and the vehicle starts to turn into the corner, right bottom plot. At the end of this period, the total drive torque has settled down to its equilibrium value related to the final steady-state powerslide motion. The virtual test driver countersteers and compensates path deviation, right top plot, with additional steering input. Obviously, the states converge to the powerslide equilibrium, which has been successfully stabilised, left middle plot.

A step-like external disturbance, represented as a reduction of the friction potential to $\mu = 0.8$, is applied at time $t = 20$ s for a duration of 0.2 s, which is equivalent to a length of 4.6 m at the current velocity. Only small yaw oscillations appear, and only small steering corrections are required from the virtual test driver while the driver assistance system robustly compensates the friction potential disturbance by vigorously adapting the drive torque distribution γ, left bottom plot in Figure 11.

4.3. Experiment

The driver assistance system was also tested in real application at different tyre–road surface conditions, on dry asphalt, wet asphalt, and packed ice ($\mu \approx 1 - 0.6 - 0.25$). The experiments were conducted with an AWD vehicle with individual electric motors at the front and the rear axles, with vehicle parameters similar to Table 1. While the vehicle sideslip angle β was measured with an external GNSS/INS system, other signals were recorded from the internal bus system of the vehicle.

To initiate the powerslide with the driver assistance system, the driver applies and keeps full throttle, starting at regular cornering conditions. The driver assistance system increases the drive torque at the rear axle to linearly ramp-up the vehicle side slip angle β to the desired vehicle side slip angle β_{des}, while the driver has to countersteer to keep the desired

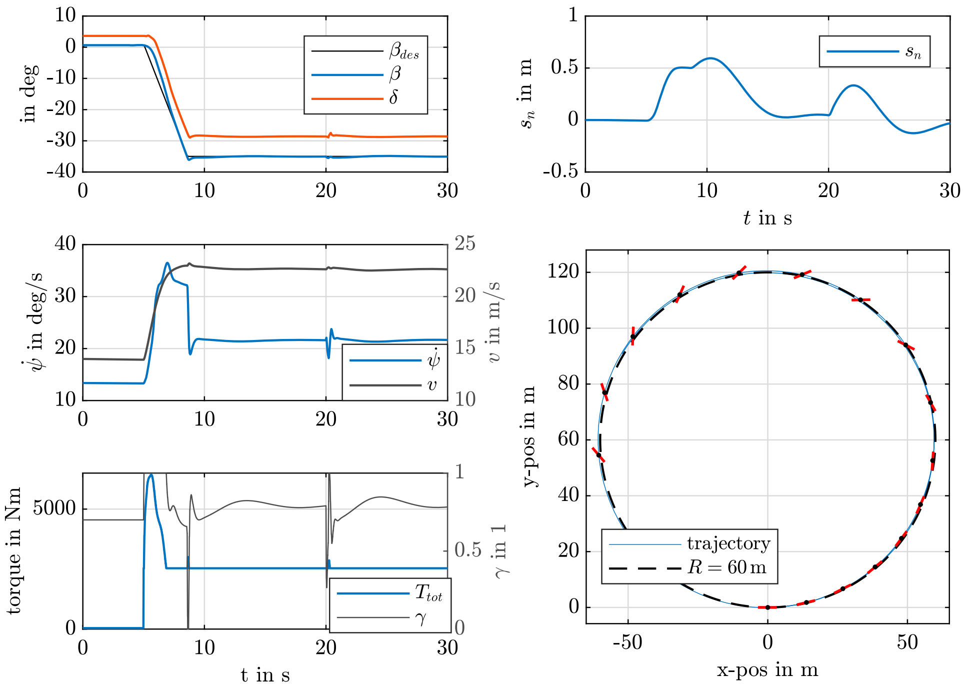

Figure 11. Simulation of powerslide initiation, stabilisation and disturbance compensation for radius $R = 60$ m, desired vehicle sideslip angle $\beta_{des} = -35°$, tyre–road friction potential $\mu = 1$; nominal drive torque distribution $\gamma_0 = 0.8$; control gains $a_1 = 40{,}000$ Nm/rad, $a_2 = 17{,}000$ Nms/rad.

reference trajectory. During the sustained powerslide, the driver assistance system controls the torque of each axle by changing parameters on the drive control unit of the vehicle to maintain the desired vehicle sideslip angle β_{des}, while the human driver tracks the reference trajectory by controlling the steering angle δ. The driver terminates the powerslide by releasing the accelerator pedal. Recovery from the powerslide to normal driving is not yet implemented and has to be accomplished by the driver, as the focus of the experiments is put on the general powerslide stabilisation task and the interaction of the proposed driver assistance system with the human driver.

In Figure 12, measurement data are presented for a powerslide manoeuvre conducted on dry asphalt. The desired vehicle sideslip angle is set to $\beta_{des} = -30°$. One can see that the controller of the driver assistance system very closely adjusts both the initial ramp and the desired constant vehicle sideslip angle. The steering angle of the human driver for tracking the circular path is quite smooth, top plot. Both the yaw rate $\dot\psi$ and the vehicle velocity v, centre plot, converge to their steady-state values. The yaw rate is oscillating, probably due to time delays in the vehicle bus system and inertial effects of the drive train, which are not considered in the simple controller.

The bottom plot of Figure 12 shows the front and rear axle torques, T_F and T_R, and the drive torque distribution γ. The drive torque distribution oscillates w.r.t. the nominal drive torque distribution $\gamma_0 \approx 0.7$. Due to the high friction potential on dry asphalt and the limited maximum motor torques of the test vehicle, the radius $R \approx 20$ m of the circular path was small at this test manoeuvre.

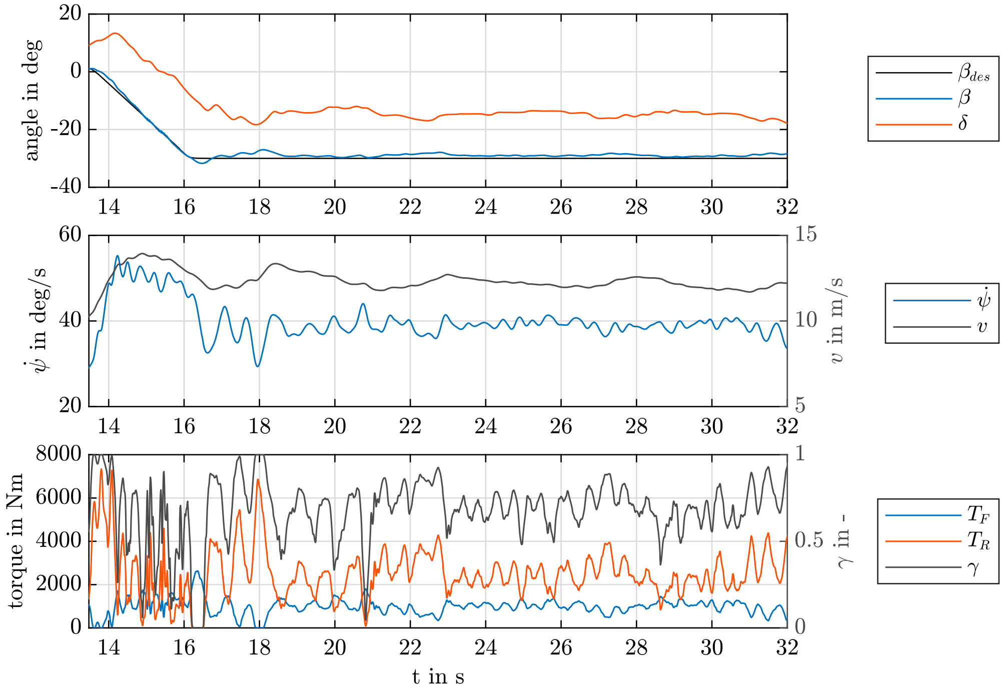

Figure 12. Measurement results from powerslide initiation and stabilisation with human driver/driver assistance system when tracking a circular path of radius $R \approx 20$ m on dry asphalt (tyre–road friction potential $\mu \approx 1$).

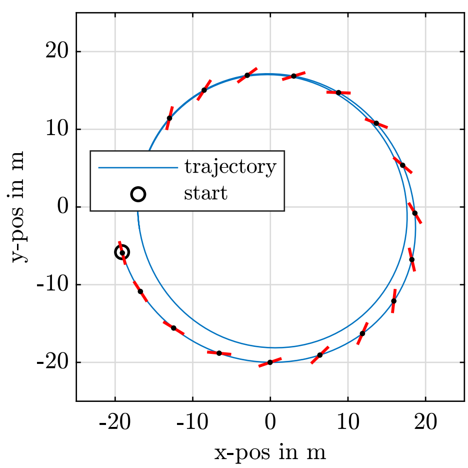

Figure 13. Measured trajectory of the *CG* of the vehicle and vehicle centre line corr. to Figure 12.

The resulting trajectory of the vehicle's centre of gravity *CG* and the vehicle position are illustrated in Figure 13. It was easy for the driver to track the circular path or eventually increase/decrease the radius, as the driver was relieved from the stabilisation task of the unstable powerslide motion.

5. Conclusions

The characteristic properties of the powerslide motion for an all-wheel drive (electric) vehicle with individual motors at the front and rear axles have been investigated. Besides the steering angle input, the effectiveness of the drive train in stabilising the unstable steady-state powerslide motion has been analysed. In addition to the steering angle and the total drive torque input, the distribution of the total drive torque between the front and rear axles is an effective 'actuator' for the stabilisation task.

The controllability analysis reveals that the control strategy for stabilising the powerslide motion with the total drive torque depends on the (nominal) drive torque distribution. With decreasing drive torque distribution front:rear (here at about 25:75), the strategy has to be changed from an 'RWD-strategy' to an 'AWD-strategy', where the total drive torque has to be increased to reduce or stabilise the yaw rate and vehicle sideslip angle, in opposite to the 'RWD-strategy'. The loss of controllability of the unstable powerslide mode with the total drive torque input indicates the (constant) drive torque distribution, where the strategy has to be changed.

Another interesting observation is that the total drive torque that stabilises the unstable 'yaw mode' and thus the vehicle sideslip angle at an AWD vehicle in powerslide motion, does not automatically stabilise the unstable 'velocity mode', in contrast to the stable velocity zero-dynamics of a RWD vehicle.

Both simulation and experimental results show that a basic (linear) PD-controller is sufficient to stabilise and maintain a powerslide motion by drive torque distribution control while the (human) driver just tracks the circular path.

To improve robustness concerning changes in the tyre–road friction potential or differences in human driver behaviour, first results from applying a machine learning-based control approach appear to be very promising, [40].

Acknowledgments

We thank the ÖAMTC Fahrtechnikzentrum Wachau for providing the track for testing and measurements. We acknowledge TU Wien Bibliothek for financial support through its Open Access Funding Program.

Disclosure statement

No potential conflict of interest was reported by the author(s).

Funding

We acknowledge TU Wien Bibliothek for financial support through its Open Access Funding Program.

References

[1] Edelmann J, Plöchl M. Handling characteristics and stability of the steady-state powerslide motion of an automobile. Regul Chaot Dyn. 2009;14(6):682–692. doi: 10.1134/S1560354709060069

[2] Edelmann J, Plöchl M. Controllability of the powerslide motion of vehicles with different drive concepts. Procedia Eng. 2017;199:3266–3271. X International Conference on Structural Dynamics, EURODYN 2017. doi: 10.1016/j.proeng.2017.09.357

[3] Velenis E, Tsiotras P, Lu J. Modeling aggressive maneuvers on loose surfaces: the cases of trail-braking and pendulum-turn. In: 2007 European Control Conference (ECC); Kos, Greece. IEEE; 2007. p. 1233–1240. doi: 10.23919/ECC.2007.7068670

[4] Velenis E, Tsiotras P. Minimum time vs maximum exit velocity path optimization during cornering. In: Proceedings of the IEEE International Symposium on Industrial Electronics, 2005. ISIE 2005; Vol. 1; Dubrovnik, Croatia; 2005. p. 355–360. doi: 10.1109/ISIE.2005.1528936

[5] Tavernini D, Massaro M, Velenis E, et al. Minimum time cornering: the effect of road surface and car transmission layout. Veh Sys Dyn. 2013;51(10):1533–1547. doi: 10.1080/00423114.2013.813557

[6] Berntorp K, Olofsson B, Bernhardsson B, et al. Models and methodology for optimal vehicle maneuvers applied to a hairpin turn. In: 2013 American Control Conference; Washington, USA; 2013. p. 2139–2146. doi: 10.1109/ACC.2013.6580152

[7] Olofsson B, Lundahl K, Berntorp K, et al. An investigation of optimal vehicle maneuvers for different road conditions. IFAC Proc Vol. 2013;46(21):66–71. doi: 10.3182/20130904-4-JP-2042.00007

[8] Acosta M, Kanarachos S, Blundell M. Vehicle agile maneuvering: from rally drivers to a finite state machine approach. In: 2016 IEEE Symposium Series on Computational Intelligence (SSCI); Athens, Greece; 2016. p. 1–8. doi: 10.1109/SSCI.2016.7850095

[9] Acosta M, Kanarachos S, Fitzpatrick ME. On full MAGV lateral dynamics exploitation: autonomous drift control. In: 2018 IEEE 15th International Workshop on Advanced Motion Control (AMC); Tokyo. IEEE; 2018. p. 529–534. doi: 10.1109/AMC.2019.8371149

[10] Stano P, Tavernini D, Montanaro U, et al. Enhanced active safety through integrated autonomous drifting and direct yaw moment control via nonlinear model predictive control. IEEE Trans Intell Veh. 2024;9(2):4172–4190. doi: 10.1109/TIV.2023.3340992

[11] Zhao T, Yurtsever E, Chladny R, et al. Collision avoidance with transitional drift control. In: 2021 IEEE International Intelligent Transportation Systems Conference (ITSC); Indianapolis, USA; 2021. p. 907–914. doi: 10.1109/ITSC48978.2021.9564496

[12] Zhao T, Yurtsever E, Rizzoni G. Justifying emergency drift control for automated vehicles. IFAC-PapersOnLine. 2022;55(24):141–148. 10th IFAC Symposium on Advances in Automotive Control AAC 2022; doi: 10.1016/j.ifacol.2022.10.275

[13] Ono E, Hosoe S, Tuan HD, et al. Bifurcation in vehicle dynamics and robust front wheel steering control. IEEE Trans Control Syst Technol. 1998;6(3):412–420. doi: 10.1109/87.668041

[14] Della Rossa F, Mastinu G, Piccardi C. Bifurcation analysis of an automobile model negotiating a curve. Veh Syst Dyn. 2012;50(10):1539–1562. doi: 10.1080/00423114.2012.679621

[15] Hindiyeh RY, Gerdes JC. Equilibrium analysis of drifting vehicles for control design. In: Dynamic Systems and Control Conference; Vol. 48920; Hollywood, USA; 2009. p. 181–188. doi: 10.1115/DSCC2009-2626

[16] Steindl A, Edelmann J, Plöchl M. Influence of tyre characteristics on periodic motions for an understeering vehicle. PAMM. 2023;22(1):e202200289. doi: 10.1002/pamm.202200289

[17] Edelmann J, Eberhart M, Steindl A, et al. Post-critical behaviour of the powerslide motion. Veh Syst Dyn. 2024. submitted.

[18] Velenis E, Frazzoli E, Tsiotras P. Steady-state cornering equilibria and stabilisation for a vehicle during extreme operating conditions. Int J Veh Auton Syst. 2010;8(2-4):217–241. doi: 10.1504/IJVAS.2010.035797

[19] Velenis E. FWD vehicle drifting control: the handbrake-cornering technique. In: 2011 50th IEEE Conference on Decision and Control and European Control Conference; Orlando, USA; 2011. p. 3258–3263. doi: 10.1109/CDC.2011.6161195

[20] Velenis E, Katzourakis D, Frazzoli E, et al. Steady-state drifting stabilization of RWD vehicles. Control Eng Pract. 2011;19(11):1363–1376. doi: 10.1016/j.conengprac.2011.07.010

[21] Werling M, Reinisch P, Gröll L. Robust power-slide control for a production vehicle. Int J Veh Auton Syst. 2015;13(1):27–42. doi: 10.1504/IJVAS.2015.070727

[22] Voser C, Hindiyeh RY, Gerdes JC. Analysis and control of high sideslip manoeuvres. Veh Syst Dyn. 2010;48(S1):317–336. doi: 10.1080/00423111003746140

[23] Chaichaowarat R, Wannasuphoprasit W. Optimal control for steady state drifting of RWD vehicle. IFAC Proc Vol. 2013;46(21):824–830. doi: 10.3182/20130904-4-JP-2042.00055
[24] Hindiyeh RY, Gerdes JC. Design of a dynamic surface controller for vehicle sideslip angle during autonomous drifting. IFAC Proc Vol. 2010;43(7):560–565. doi: 10.3182/20100712-3-DE-2013.00160
[25] Goh JY, Gerdes JC. Simultaneous stabilization and tracking of basic automobile drifting trajectories. In: 2016 IEEE Intelligent Vehicles Symposium (IV); Gothenburg, Sweden; 2016. p. 597–602. doi: 10.1109/IVS.2016.7535448
[26] Goh JY, Goel T, Christian Gerdes J. Toward automated vehicle control beyond the stability limits: drifting along a general path. J Dyn Syst Meas Control. 2019;142(2):021004. doi: 10.1115/1.4045320
[27] Goh JY, Thompson M, Dallas J, et al. Beyond the stable handling limits: nonlinear model predictive control for highly transient autonomous drifting. Veh Syst Dyn. 2024;62(10):2590–2613. doi: 10.1080/00423114.2023.2297799
[28] Goel T, Goh JY, Gerdes JC. Opening new dimensions: vehicle motion planning and control using brakes while drifting. In: 2020 IEEE Intelligent Vehicles Symposium (IV); Las Vegas, USA; 2020. p. 560–565. doi: 10.1109/IV47402.2020.9304728
[29] Hou X, Zhang J, Ji Y, et al. Autonomous drift controller for distributed drive electric vehicle with input coupling and uncertain disturbance. ISA Trans. 2022;120:1–17. doi: 10.1016/j.isatra.2021.03.009
[30] Nakano H, Okayama K, Kinugawa J, et al. Control of an electric vehicle with a large sideslip angle using driving forces of four independently-driven wheels and steer angle of front wheels. In: 2014 IEEE/ASME International Conference on Advanced Intelligent Mechatronics; Besacon, France; 2014. p. 1073–1078. doi: 10.1109/AIM.2014.6878223
[31] Pacejka H. Tire and vehicle dynamics. 2nd ed. Oxford: Elsevier; 2005.
[32] Plöchl M, Edelmann J. Driver models in automobile dynamics application. Veh Syst Dyn. 2007;45(7-8):699–741. doi: 10.1080/00423110701432482
[33] Hamdan AMA, Nayfeh AH. Measures of modal controllability and observability for first- and second-order linear systems. J Guid Control Dyn. 1989;12(3):421–428. doi: 10.2514/3.20424
[34] Choi JW, Lee JG, Kim Y, et al. Design of an effective controller via disturbance accommodating left eigenstructure assignment. J Guid Control Dyn. 1995;18(2):347–354. doi: 10.2514/3.21390
[35] Lunze J. Regelungstechnik 2. Berlin, Heidelberg: Springer Vieweg; 2016.
[36] Milani S, Marzbani H, Jazar RN. Vehicle drifting dynamics: discovery of new equilibria. Veh Syst Dyn. 2022;60(6):1933–1958. doi: 10.1080/00423114.2021.1887499
[37] Edelmann J, Plöchl M, Reinalter W, et al. A passenger car driver model for higher lateral accelerations. Veh Syst Dyn. 2007;45(12):1117–1129. doi: 10.1080/00423110701203644
[38] Mitschke M, Wallentowitz H. Dynamik der Kraftfahrzeuge. Berlin, Heidelberg: Springer Vieweg; 2004.
[39] Abdulrahim M. On the dynamics of automobile drifting. SAE Technical Paper; 2006.
[40] Jaumann F, Schuster T, Unterreiner M, et al. Powerslide control with deep reinforcement learning. In: Mastinu G, Braghin F, Cheli F, et al., editors. 16th International Symposium on Advanced Vehicle Control; Cham. Springer Nature Switzerland; 2024. p. 862–868. doi: 10.1007/978-3-031-70392-8_121